



CoCo2

Prototype system for a
Copernicus CO₂ service

D3.1 Progress on developing the global transport model, data assimilation, and preliminary demonstration of CO2MVS capacity

Agusti-Panareda, Bousserez, McNorton

coco2-project.eu



Co-ordinated by
 **ECMWF**





CoCO2

Prototype system for a
Copernicus CO₂ service

D3.1 Progress on developing the global transport model, data assimilation, and preliminary demonstration of CO2MVS capacity

Dissemination Level: Public

Author(s): A.Agusti-Panareda, N.Bousserez,
G. Balsamo, L.Cantarello, M.Choulga, M.Diamantakis, R.Engelen,
J.Flemming, Z. Kipling, S. Massart, J.McNorton (ECMWF)
M. Guevara (BSC), Hugo Denier van der Gon (TNO)

Date: 25/02/2022

Version: 1.0

Contractual Delivery Date: 31/12/2021

Work Package/ Task: WP3/ T3.1

Document Owner: ECMWF

Contributors: ECMWF

Status: Final



CoCO2: Prototype system for a Copernicus CO₂ service

Coordination and Support Action (CSA)
H2020-IBA-SPACE-CHE2-2019 Copernicus evolution –
Research activities in support of a European operational
monitoring support capacity for fossil CO₂ emissions

Project Coordinator: Dr Richard Engelen (ECMWF)
Project Start Date: 01/01/2021
Project Duration: 36 months

Published by the CoCO2 Consortium

Contact:
ECMWF, Shinfield Park, Reading, RG2 9AX,
richard.engelen@ecmwf.int



The CoCO2 project has received funding from the European Union's Horizon 2020 research and innovation programme under grant agreement No 958927.



Table of Contents

| | | |
|-------|---|----|
| 1 | Executive Summary | 7 |
| 2 | Introduction | 7 |
| 2.1 | Background | 7 |
| 2.2 | Scope of this deliverable | 7 |
| 2.2.1 | Objectives of this deliverable | 7 |
| 2.2.2 | Work performed in this deliverable | 7 |
| 2.2.3 | Deviations and counter measures | 8 |
| 3 | Transport model developments | 8 |
| 3.1 | Testing the flexible emission framework | 8 |
| 3.2 | IFS simulations | 9 |
| 3.3 | Global mass conservation | 10 |
| 3.4 | Plume simulations | 12 |
| 4 | Data assimilation developments | 16 |
| 4.1 | Methodology | 16 |
| 4.2 | Workplan | 17 |
| 4.3 | Short-window variational inversion | 18 |
| 4.4 | Ensemble of Data Assimilation (EDA) | 18 |
| 5 | Demonstration of CO ₂ MVS capability | 19 |
| 5.1 | Demonstration using CH ₄ | 20 |
| 5.1.1 | Regional Emissions – Permian Basin, USA | 20 |
| 5.1.2 | Point Source Emissions – Appin Colliery, Australia | 21 |
| 5.1.3 | Blowout Event – Eagle Ford, USA | 22 |
| 5.1.4 | 1-day Regional Emissions – Silesian Basin, Europe | 24 |
| 5.1.5 | The Impact of Covid-19 on Emissions | 25 |
| 5.2 | Demonstration Using NO _x | 26 |
| 5.2.1 | NO _x Emissions – Bełchatów Power Station, Poland | 27 |
| 6 | Conclusion | 28 |
| 7 | References | 29 |

Figures

| | |
|---|----|
| <i>Figure 1 Diurnal cycle of emission sectors from CAMS-TEMPO (Guevara et al., 2021)</i> | 9 |
| <i>Figure 2 Cumulative global mass conservation error associated with the different experiments listed in Table 1 for CO₂ (upper panel) and CH₄ (lower panel)</i> | 11 |

| | |
|---|----|
| Figure 3 XCO ₂ enhancement [ppm] in magenta-brown colours from four simulations. CO ₂ observations of the Berlin plume from Klausner et al. (2020) are shown as coloured circles (see colour bar on upper right-hand side of each panel). Note that there are no column observations from this case study. The black triangle depicts the location of Jänschwalde power station (Germany)..... | 13 |
| Figure 4 XCH ₄ enhancement [ppb] in magenta-brown colours from four simulations. CH ₄ observations of the Berlin plume from Klausner et al. (2020) are shown as coloured circles (see colour bar on upper right-hand side of each panel). | 14 |
| Figure 5 Relative difference [%] in the anthropogenic emission enhancement for XCO ₂ and XCH ₄ associated with (a,b) COMADH (compared to standard SL); (c,d) 9km resolution (compared to 25km resolution); and (e,f) the use of emission heights and diurnal cycle for the various anthropogenic emission sectors. The black triangle depicts the location of Jänschwalde power station (Germany)..... | 15 |
| Figure 6 Schematic of the ensemble-variational inversion system that enables to extend the current short-window 12-hour 4D-Var capability (purple) to longer timescale (i.e., days to weeks)..... | 17 |
| Figure 7 Schematic and timeline of the workflow to implement the global IFS CO ₂ MVS. | 18 |
| Figure 8 Horizontal error correlation length scales (km) for CO ₂ molar fraction at model level 95 (~500hPa) as diagnosed by a wavelet-based B matrix representation. The wavelet-B matrix is constructed based on error statistics derived from the EDA system. | 19 |
| Figure 9 Schematic of different resolutions used in the inversion shown by pseudo-data for 5 sectors. The magnitude of prior emissions at ~9 km (left) and as input to the forward model at ~25 km (middle). The inversion increment at ~80 km, resulting scaling factors are applied to all sectors within the grid cell, the boxes indicate relative contribution per sector (right). b) Schematic of inversion setup using the 24-hour window, correcting for the initial 3D state, emissions, and initial conditions in the prior of the subsequent window. (McNorton et al., 2022). | 20 |
| Figure 10 a) Average prior Permian Basin CH ₄ emissions for 2019. b) Average of posterior minus prior anthropogenic CH ₄ emissions over the Permian Basin for January-June 2019, excluding days for which observations were not available. c) Time series of total prior (black circles) and posterior (green triangles) anthropogenic CH ₄ emission estimates within the 6°x4° Permian Basin domain, centered around 32°N, 103°W (black box in b) for 2019-2020, excluding days for which observations were not available. (McNorton et al., 2022)..... | 21 |
| Figure 11 a) The sector specific contribution to emissions within the Appin Colliery domain. b) Time series of total prior (black circles) and posterior (green triangles) CH ₄ emission estimates within the domain for 2019-2020, excluding days for which observations were not available. c) Prior CH ₄ emissions for January 2019, the white box denotes the grid cell used to estimate emissions. d) Average posterior minus prior CH ₄ emissions for 2019, excluding days for which observations were not available. (McNorton et al., 2022). | 22 |
| Figure 12 a) Prior (black circles) and Posterior (green triangles) anthropogenic CH ₄ emission estimates, where observations are available, over an oil well blowout event in Eagle Ford, USA during October/November 2019 at the grid scale (a) and within a 4°x4° domain (b). The nearest date (2nd November) to the event, which occurred on the 1st November, is indicated. Regional scaling factor values from the inversion for November 1st (C), 2nd (D) and 3rd (E). Eagle Ford blowout site marked with an 'x' and 4°x4° domain denoted. (McNorton et al., 2022). | 23 |
| Figure 13 a) The Upper Silesian Coal Basin 1°x0.5° domain indicated by the white box, centred around 50.0°N, 18.7°E. Also shown are eleven major coal mines in the region (© Google Maps, 2021). b) Time series of total prior (black circles) and posterior (green triangles) CH ₄ emission estimates within the domain for 2019-2020, where observations and inverse simulations were available. c) Prior total CH ₄ emissions for 6th June 2018. d) Average posterior minus prior CH ₄ emissions for 6th June 2018. (McNorton et al., 2022)..... | 24 |

| | |
|--|----|
| Figure 14 <i>Estimated national/regional average CH₄ emission change between 2020 and 2019 for January to June, derived using an IFS inversion for the largest emitters for a) Energy, b) Agriculture, c) Waste and d) Other Anthropogenic sources. e) Global change in sector specific monthly CH₄ emissions for the same period. f) National/regional change in total anthropogenic CH₄ emissions for the same period. (McNorton et al., 2022).</i> | 26 |
| Figure 15 <i>Map of the 3 case studies highlighted in WP4 for investigation (© Google Maps, 2021).</i> | 26 |
| Figure 16 <i>Simulated total column NO₂ for a 24-hour period (7th June, 2018) from the IFS global prototype over Western Poland. The green box denotes the location of the Bełchatów power station.</i> | 27 |
| Figure 17 <i>Prior anthropogenic NO_x emissions for Western Poland in June, 2018 taken from the CAMS inventory (top). The difference in NO_x emissions for the same region and period between inverse and prior estimates, when assuming no correlation between NO_x and CO₂ emissions (bottom). The green box denotes the location of the Bełchatów power station.</i> | 28 |

Tables

| | |
|---|----|
| Table 1: <i>List of IFS simulations with different configuration. All the simulations use the same underlying anthropogenic emissions (CAM5-GLOB-ANTv5.1 based on EDGARv5). All the simulations use the LQM3D quasi-monotonic filter.</i> | 10 |
|---|----|

1 Executive Summary

The global CO₂ Monitoring Verification System (CO₂ MVS) of the Copernicus CO₂ Service will use the Integrated Forecasting System (IFS) at ECMWF to estimate global anthropogenic emissions of CO₂ and CH₄. This requires the development of the inversion capability in the IFS including CO₂, CH₄ and co-emitted species, the use of a long window for data assimilation and a mass conserving tracer transport advection scheme. This report describes the progress on these different aspects during the first 12 months of the CoCO₂ project. We use case studies, focusing on simulations of plumes and CH₄ inversion studies to showcase the capability of the IFS towards the estimation of fossil fuel emissions at global scale. The main achievements presented include: (i) the use of a new interpolation method COMADH resulting in a much better mass conservation of CO₂ and CH₄ in the tracer transport model; (ii) the implementation of a simplified chemistry tangent-linear adjoint (TL-AD) code in the IFS analysis and inversion system; (iii) a demonstration of the IFS inversion capability with CH₄ fluxes for several published case studies.

2 Introduction

2.1 Background

The global IFS model and its data assimilation capabilities will serve as the basis to build the future global CO₂ MVS. Developments entail improvements of both the transport model to accurately represent CO₂ plumes originating from anthropogenic sources (Section 3) and the current 4D-Var IFS data assimilation system to adapt it to GHG inversions. In particular, the current short-window (12-hour) configuration of the IFS operational system needs to be extended to assimilate observations at time scales suitable for long-lived tracers such as CO₂ (i.e., several days to month) (Section 5). Additionally, prior information (i.e., emission inventories and associated prior uncertainties) produced in WP2 needs to be evaluated before their uptake in the global CO₂ MVS along with the constraints provided by available and future atmospheric observations. The latter can be achieved by constructing a so-called nature run which represents the best available simulation of the true state of the atmosphere, and from which Observation Simulation System Experiments (OSSEs) can be performed (Section 4). Lastly, a continuous evaluation of the system developments during the project is required to assess and address its limitations and best allocate research efforts towards building the pre-operational CO₂ MVS (Section 6).

2.2 Scope of this deliverable

2.2.1 Objectives of this deliverable

This deliverable report outlines the latest developments for the global transport capacity of the IFS and its data assimilation. The development includes tests of the advection improvements, state vector, assimilation windows, covariance treatment, implementation of the new emission inversion capacity in the IFS prototype, and a list of research priorities and development tasks to be considered under the umbrella of Copernicus.

2.2.2 Work performed in this deliverable

The work is divided into three parts:

- Section 3 presents the testing of a new advection scheme and improved representation of emissions in the IFS that will be implemented in the next CAMS IFS cycle to be also

used in the CoCO₂ nature runs. The tests focus on the simulation of plumes from emission hotspots, in particular on a study of a plume from Berlin during the O3D field campaign, as documented by Klausner et al. (2020).

- Section 4 describes the data assimilation developments in the IFS.
- Section 5 presents a demonstration of the IFS inversion capabilities and progress.

2.2.3 Deviations and counter measures

N/A

3 Transport model developments

Atmospheric tracer transport is crucial to interpret the atmospheric CO₂ observations and to estimate the surface sources and sinks from those observations. Transport encompasses a wide range of temporal and spatial scales, from meters and seconds (turbulent motions in plumes from point sources) to thousands of kilometres and multi-annual scales in the inter-hemispheric mixing and the troposphere-stratosphere exchange. The overall CO₂MVS capacity is required to model accurately all those scales from plumes at hourly scales to global growth rate at annual scales. While this will be addressed by using modelling and data assimilation systems at different scales (local to global), one of the big challenges is that we still need very high spatial and temporal resolution at global scale which is computationally very expensive.

The IFS transport model is based on the semi-Lagrangian (SL) advection scheme which allows to transport multiple tracers accurately, stably and efficiently (using long timesteps) at a relatively high resolution globally (9km in the current operational configuration and 4km in development). However, SL advection schemes have the limitation that they do not conserve mass. For this reason, the CAMS atmospheric composition forecast uses a mass fixer to correct for the mass conservation error (Diamantakis and Flemming, 2014; Agusti-Panareda et al., 2017; Diamantakis and Agusti-Panareda, 2017). Although this works satisfactorily for atmospheric analysis and forecasts, the use of a mass fixer near surface emission sources and sinks can be problematic for an inversion system. Therefore, it is desirable to limit the action of the mass fixer in these regions as much as possible. In a SL scheme, the main cause of tracer mass conservation error is the method used to interpolate the transported fields at the departure points of the trajectories their constituent parcels follow within one timestep. Malardel and Ricard (2015) developed an alternative semi-Lagrangian interpolation method to address the problem of grid-point storms in NWP models, a problem linked with the inability of the SL methods to conserve mass locally. This new method of interpolating at the departure points is known as COMAD (**C**ontinuous **M**apping about **D**eparture points). It works by modifying the standard interpolation weights considering the deformation of the advected air parcels due to flow convergence/divergence. This modification improves mass conservation especially in regions of light converging winds near the surface (a typical scenario that gives large local mass conservation errors). Here we use COMAD-Horizontal (COMADH) for the horizontal interpolation at the departure point. COMADH is compared to the standard SL advection scheme in simulations of CO₂ and CH₄ at various resolutions.

3.1 Testing the flexible emission framework

In addition to the new COMADH Semi-Lagrangian (SL) advection scheme, the IFS has now a flexible emission framework where the sectorial emissions can have different temporal and vertical profiles. This framework ensures consistency between species that have emissions from the same sector. The temporal profiles for the diurnal cycle of the anthropogenic emissions sectors used in the IFS are shown in Fig. 1.

Table 1: List of IFS simulations with different configuration. All the simulations use the same underlying anthropogenic emissions (CAM5-GLOB-ANTv5.1 based on EDGARv5). All the simulations use the LQM3D quasi-monotonic filter.

| IFS simulations | Resol | Emission Diurnal cycle | Emission heights | Advection scheme | Mass fixer |
|---------------------------|-------|------------------------|------------------|--------------------------|------------|
| 9km_COMADH_MF_emis_H_DC | 9km | Yes | Yes | COMADH | Yes |
| 25km_COMADH_MF_emis_H_DC | 25km | Yes | Yes | COMADH | Yes |
| 9km_COMADH_noMF_emis_H_DC | 9km | Yes | Yes | COMADH | No |
| 9km_SL_MF_emis_H_DC | 9km | Yes | Yes | Standard semi-Lagrangian | Yes |
| 25km_SL_MF_emis_H_DC | 25km | Yes | Yes | Standard semi-Lagrangian | Yes |
| 9km_SL_noMF_emis_H_DC | 9km | Yes | Yes | Standard semi-Lagrangian | No |
| 9km_COMADH_MF | 9km | No | No | COMADH | Yes |
| 9km_COMADH_MF_emis_DC | 9km | Yes | No | COMADH | Yes |
| 9km_SL_MF | 9km | No | No | Standard semi-Lagrangian | Yes |

3.3 Global mass conservation

Global mass conservation is an important prerequisite for modelling long-lived greenhouse gases. The standard SL scheme used in the IFS is not mass conserving. Although the error at each model time step is small, it is systematic and it accumulates with time, reaching values that are comparable to the annual growth rates of CO₂ and CH₄ after one year of simulation (Agusti-Panareda et al., 2017). Figure 1 shows the accumulation of the global mass conservation error for a week, comparing different configurations for the advection scheme. High resolution results in a larger cumulative mass conservation error because it has a smaller time step and therefore the error accumulates faster (Agusti-Panareda et al. 2017). However, for COMADH the difference between the mass conservation between the 9km and 25km is very small for CO₂ as shown by the red and blue lines in the upper panel of Fig. 2. Other factors that influence the mass conservation error are the diurnal cycle of emissions and the emission injection heights. The diurnal cycle is particularly important for improving the mass conservation (see yellow and grey lines in upper panel of Fig.2). This is because with the inclusion of the diurnal cycle the emissions have lower values during night-time when there is less atmospheric mixing. This leads to a reduction in the atmospheric tracer gradients and therefore to smaller errors in the semi-Lagrangian interpolation of the transported fields at the departure points. The increase of emission injection height also leads to a reduction of the tracer gradients because the wind speed and mixing in the boundary layer generally increases with height.

The global CO₂ mass conservation error is 0.024 ppm/week in the standard SL advection (9km_SL_emisHandDC) experiment and 0.007ppm/week in the COMADH advection (9km_COMADH_emisHandDC) experiment. For CH₄ the error reduction is smaller, from

0.41ppb/week (9km_SL_emisHandDC) to 0.24ppb/week (9km_COMADH_emisHandDC). This means that for the IFS inversions with DA window of 12 hours to a month (in hybrid ensemble-variational system) there is no need for using a mass fixer, as the mass conservation with COMADH is small enough (i.e. smaller than the accuracy of assimilated observations).

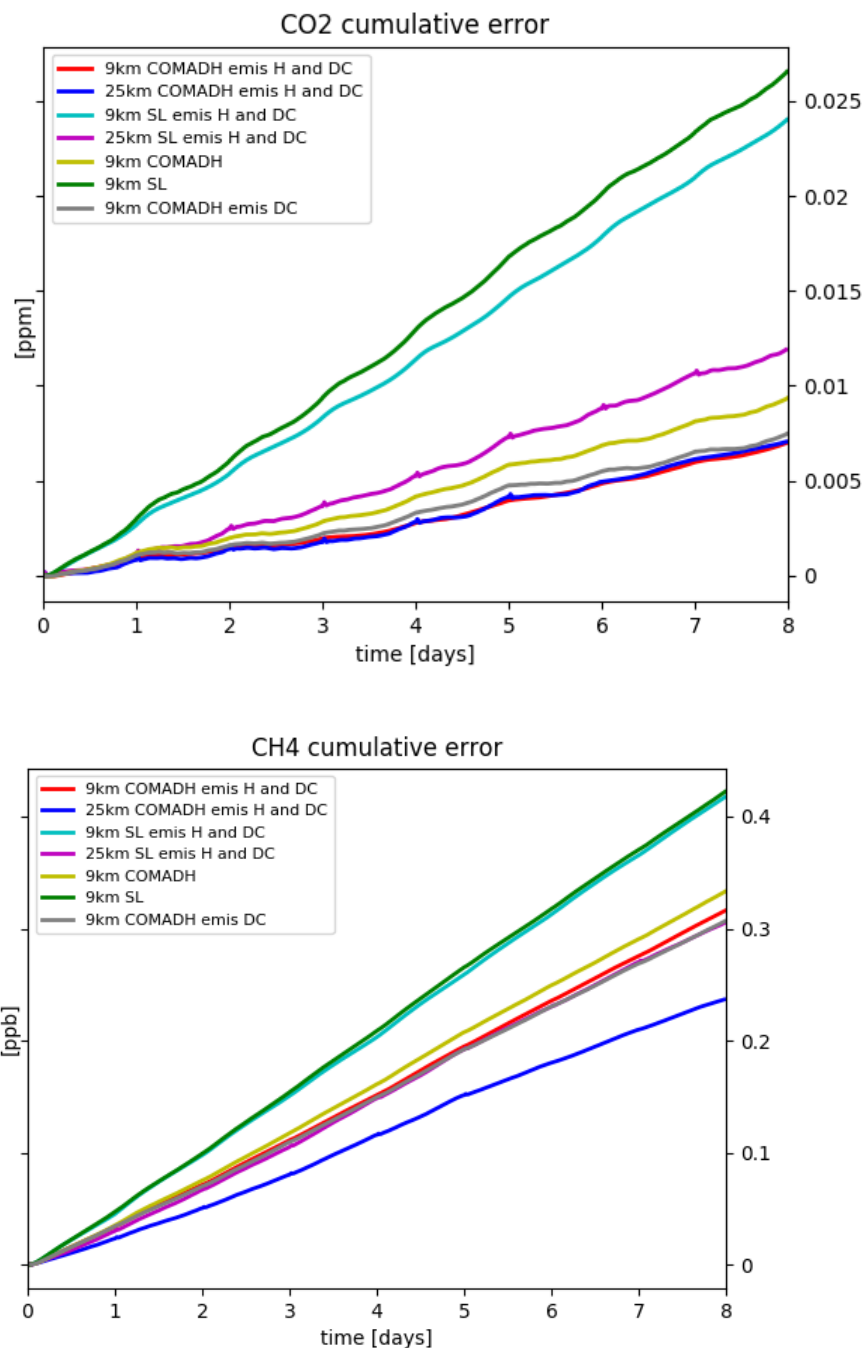


Figure 2 Cumulative global mass conservation error associated with the different experiments listed in Table 1 for **CO₂** (upper panel) and **CH₄** (lower panel).

3.4 Plume simulations

In this section we look at the impact the transport model improvements and emission temporal/vertical profiles listed in section 3.2 on the simulation of plumes from emission hotspots. We focus on a case study of a plume from Berlin on 20 July 2018 (Klausner et al., 2020). Figures 3 and 4 show the simulated plume as column-averaged molar fraction enhancements emanating from Berlin for the various simulation experiments from 0 to 12 UTC. The flight campaign CO₂ and CH₄ observations from Klausner et al. (2020) have been over-plotted to assess the model simulations. The location of both CO₂ and CH₄ plumes coincides with the observed high values of CO₂ and CH₄ along the southern section of the flight track. There are also differences between the different simulations, which can be subtle in the case of the advection scheme. Figure 5 shows the impact of the COMADH advection scheme, high resolution and emission heights and diurnal cycles directly by plotting the difference between the relevant experiments. A list of the main findings is provided below:

- There is generally a lower tracer enhancement associated with COMADH (from 2 to 15%) in the Berlin plume as well as other anthropogenic plumes (Fig. 4a, b). This is consistent with the lower positive mass conservation error compared to the standard semi-Lagrangian scheme shown in Fig. 2.
- Increasing the horizontal resolution from 25km (as in CAMS GHG analysis) to 9km (as in NWP forecast or CAMS high resolution forecast) results in an increase of 30 to 50 % in the maximum CO₂ enhancement caused by anthropogenic emissions. Further simulations are in progress to assess the impact of increasing the resolution from 9km to 4km.
- The impact of including the diurnal cycle and vertical profile of emissions is different for CO₂ and CH₄ because they are affected by different sectors with different diurnal cycles and emission heights. There is an overall increase of CO₂ from 0 to 12 UTC near Berlin and other cities with the diurnal cycle of the traffic and residential heating emissions which peak in the morning (Fig. 1). In contrast, further downstream there is an overall decrease in the column enhancement associated with the emission heights with stronger winds providing faster mixing of the plume with the background air. This is also the case for CH₄, with lower values along most of the plume and larger values at the edge of the plume indicating a longer extension of the plume associated with the faster transport. As the wind direction can vary with height, the orientation of the plume can also change when comparing simulations with and without injection height. This is the case for the plume from Jämschwalde power plant (Figs 3a,d and Figure 5e).

These results show the IFS is able to simulate plumes from cities at 9km but there is a very large impact from model resolution and temporal/vertical emission profiles on the simulated CO₂ and CH₄ plumes. Thus, further study is required to evaluate more plume case studies with observations and with other higher resolution regional models in collaboration with WP4.

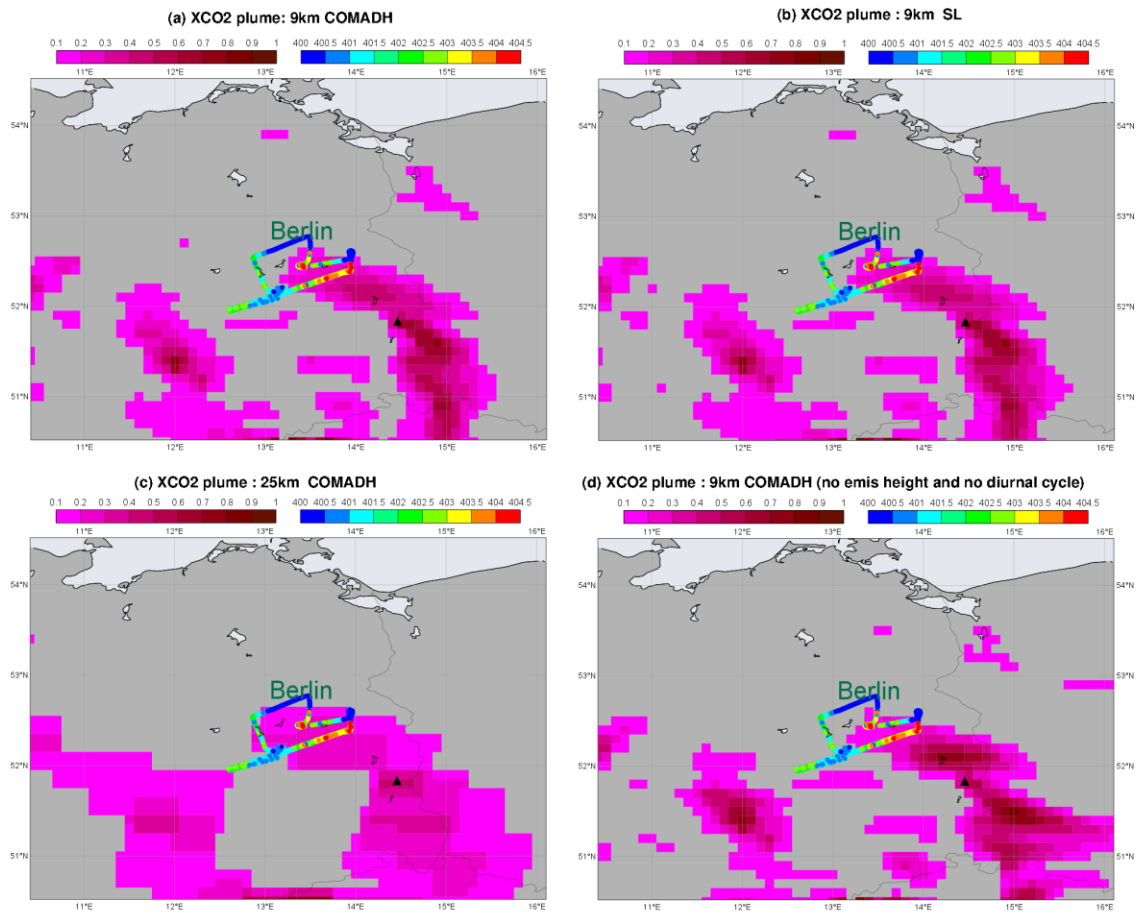


Figure 3 XCO₂ enhancement [ppm] in magenta-brown colours from four simulations. CO₂ observations of the Berlin plume from Klausner et al. (2020) are shown as coloured circles (see colour bar on upper right-hand side of each panel). Note that there are no column observations from this case study. The black triangle depicts the location of Janschwalde power station (Germany).

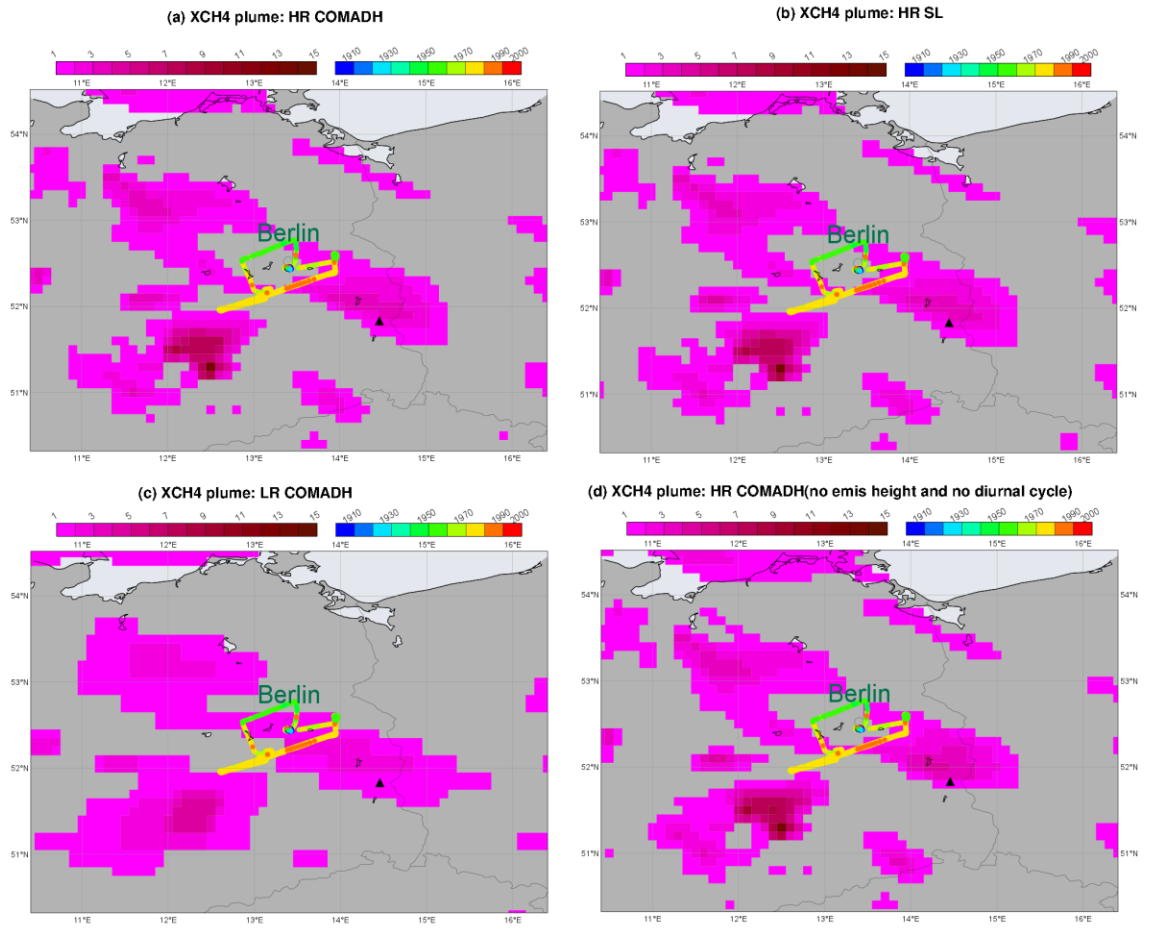


Figure 4 XCH₄ enhancement [ppb] in magenta-brown colours from four simulations. CH₄ observations of the Berlin plume from Klausner et al. (2020) are shown as coloured circles (see colour bar on upper right-hand side of each panel).

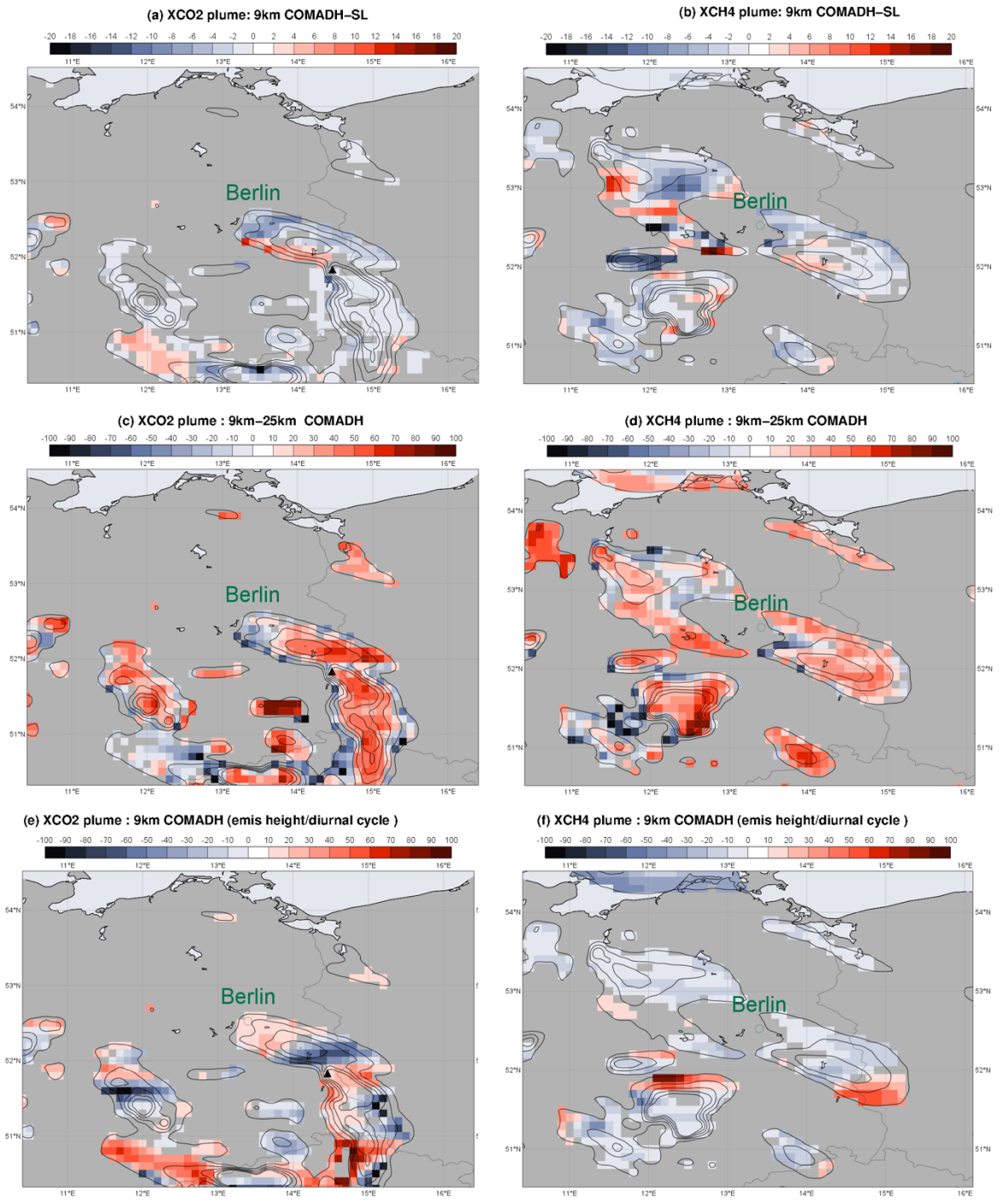


Figure 5 Relative difference [%] in the anthropogenic emission enhancement for XCO₂ and XCH₄ associated with (a,b) COMADH (compared to standard SL); (c,d) 9km resolution (compared to 25km resolution); and (e,f) the use of emission heights and diurnal cycle for the various anthropogenic emission sectors. The black triangle depicts the location of Jämschwalde power station (Germany).

4 Data assimilation developments

A first version of the global CO₂ emission inversion system has been implemented in the IFS. It consists of a short-window (24-hour) 4D-Var inversion that is a fundamental building block of the future Copernicus CO₂ MVS. The sections below describe the general approach chosen (Section 4.1), the workplan for its implementation (Section 4.2), as well as the characteristics of the current short-window variational prototype.

4.1 Methodology

The chosen methodological approach to build a CO₂ emission inversion system is described in a draft manuscript that can be found here: <https://arxiv.org/abs/1910.11727>. This document is under revision to account for recent progresses made in the design of the prototype. The prototype global CO₂MVS shall accommodate several constraints, including the need for consistent integration in the existing operational IFS framework and the computational efficiency necessary to meet near-real time delivery requirements for the future Copernicus service (CAMS 2.0). In that context, a hybrid ensemble-variational method has been designed that blends the existing variational algorithm with ensemble-based techniques to:

1. Include chemical processes in the 4D-Var minimisation (inner-loop) without the need to use costly full chemistry TL/adjoint models.
2. Extend the current IFS operational 12-hour 4D-Var window capability to perform long-window (i.e., several weeks) 4D-Var GHG inversions.

In a nutshell, the implicit propagation of the background error covariance in the minimisation through the TL/adjoint integrations is combined with an (explicit) ensemble-based covariance estimate. This modification enables to include, e.g., chemistry processes in the inner-loop using a small ensemble of full-chemistry forward integrations. Additionally, the 4D-Var window can be extended to several days or weeks based on ensemble-based estimation of the correlation between the initial states of GHG species and emissions from previous windows. That step only requires to generate and store an ensemble of CO₂ and CH₄ trajectories for each 4D-Var cycle. Figure 6 provides a schematic of the ensemble-variational system.

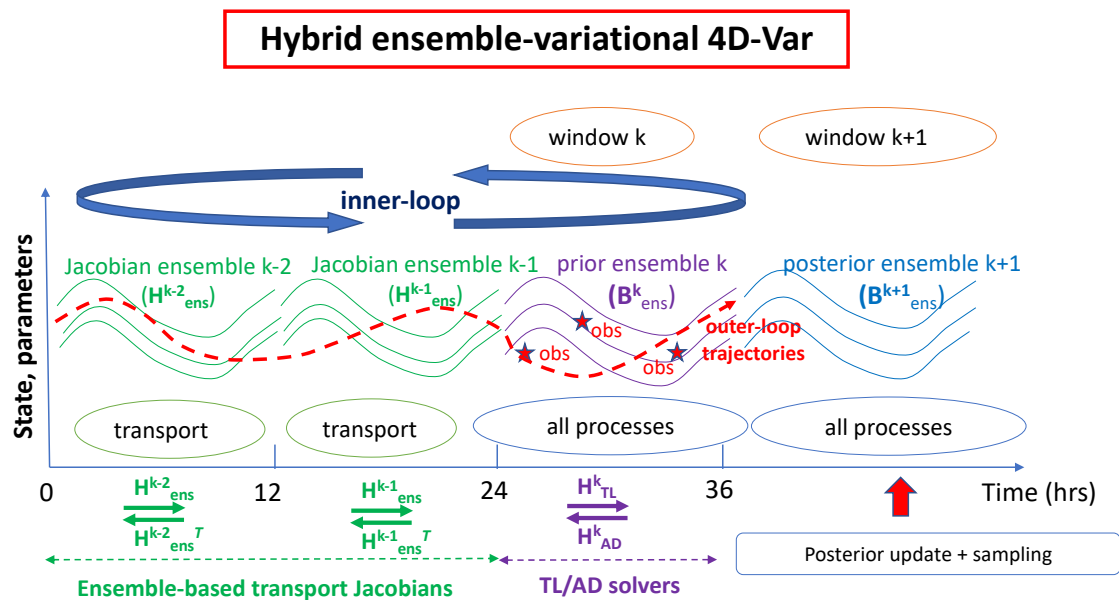


Figure 6 Schematic of the ensemble-variational inversion system that enables to extend the current short-window 12-hour 4D-Var capability (purple) to longer timescale (i.e., days to weeks).

4.2 Workplan

Building a global IFS CO₂ source inversion system following the methodological approach outlined in Section 4.1 involves many steps, some of which can be performed in parallel. The milestones are:

1. Development of a prototype emission inversion system in the current operational IFS 4D-Var
2. Merging of the IFS emission inversion developments with the future operational object-oriented OOPS-IFS 4D-Var system after the end of the CoCO₂ project.
3. Development of an Ensemble of Data Assimilation (EDA) system for OSSE-based evaluation and error propagation capabilities.
4. Combination of the ensemble system with the OOPS variational system to implement a hybrid ensemble-variational algorithm that enables:
 - a. Long-window GHG source inversions
 - b. Inner-loop minimisations that include chemical processes

Figure 7 provides an approximate timeline for the technical implementation of the prototype IFS CO₂ inversion system with an emphasis on the three main components of the work, i.e., short-window IFS 4D-Var, OOPS implementation, ensemble system, and their connections.

IFS data assimilation developments

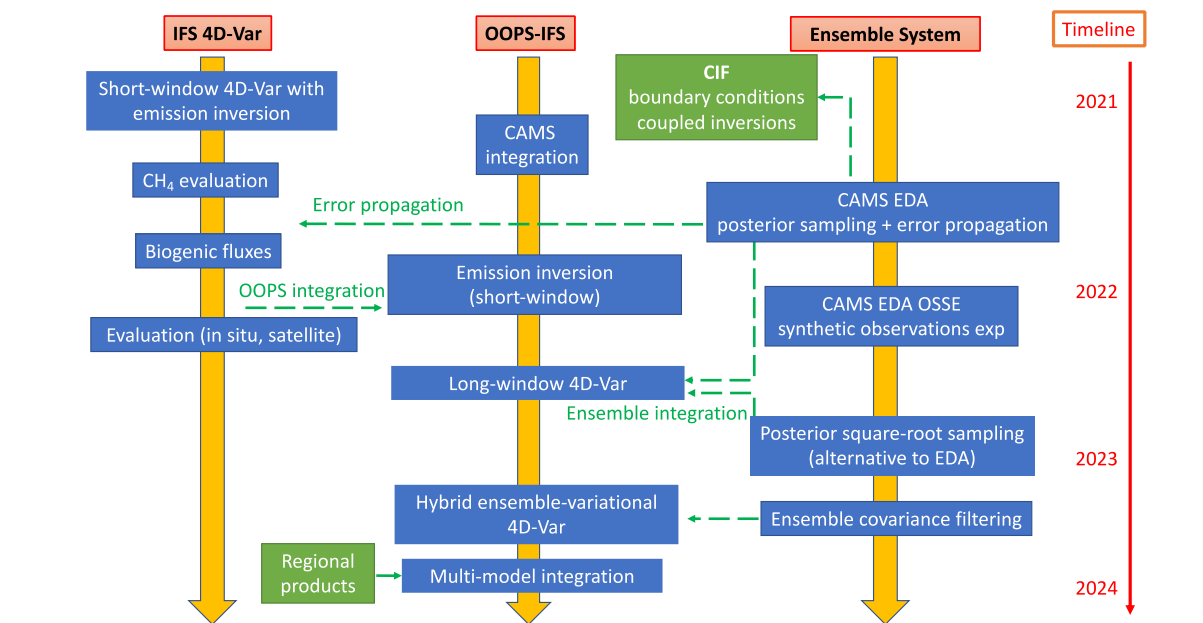


Figure 7 Schematic and timeline of the workflow to implement the global IFS CO₂ MVS.

4.3 Short-window variational inversion

The current capability of the global IFS prototype inversion system is as follows:

- 24-hour 4D-Var window
- Joint optimisation of greenhouse gas and reactive species emissions together with initial conditions.
- Optimised emissions: CO₂, CH₄, NO and CO.
- TL/AD models of simplified chemistry scheme (photochemical equilibrium)
- Prior error definition:
 - Global constant or 2D map of standard errors
 - Spatial error correlation length scales (via wavelet **B**)
 - NO/CO₂ emission error correlations in **B** (enables NO₂ observation constraints on CO₂ emissions)

4.4 Ensemble of Data Assimilation (EDA)

As part of the tools developed to evaluate the emission inversion system, an EDA-based OSSE is being implemented. The idea is to complement OSSEs based on the CoCO₂ IFS nature run with a statistical analysis exploiting the available EDA system.

The rationale behind the EDA-based OSSE system is to provide a statistical Monte-Carlo evaluation of the prototype performance, by generating many samples of the posterior emissions that can be compared to known "true" emissions. In short, pseudo-observations are first generated from a known "true" emission inventory. The emission inventory and the pseudo-observations are then perturbed according to their respective error statistics and used to produce a set of posterior emission estimates. This posterior ensemble can then be used to estimate posterior errors and the information content of the inversion (i.e., model resolution matrix), as well as to perform sensitivity analyses to quantify the impact of, e.g.,

uncertainties in prescribed background emission error covariances, transport model biases and errors on the performance of the inversion.

As a first step towards the implementation of an EDA that includes posterior emission statistics, the current IFS EDA has been extended to include chemical 3D state information. Figure 8 shows preliminary results of horizontal error correlation length scales for CO₂ mole fraction at around 500hPa diagnosed by the IFS wavelet-B model representation using the EDA ensemble statistics. As expected, the correlation length scales are largest in the tropics and smallest at northern mid-latitudes near emission hotspots and at high latitudes. The ability of the wavelet model to represent heterogeneous spatial error correlation will be exploited when modelling the prior error covariance matrix. This work is also linked to the development of mechanisms to transfer information from global to local scales in WP5 (Task 5.3.1).

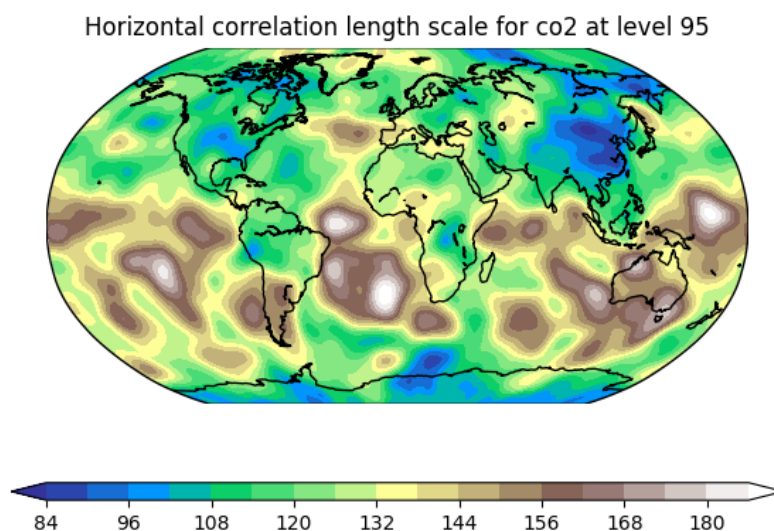


Figure 8 Horizontal error correlation length scales (km) for CO₂ molar fraction at model level 95 (~500hPa) as diagnosed by a wavelet-based B matrix representation. The wavelet-B matrix is constructed based on error statistics derived from the EDA system.

5 Demonstration of CO₂MVS capability

Initial developments on the global IFS system have focused on the implementation of a short-window (24-hour) 4D-Var inversion, coupling the current NWP system with the optimisation of trace gas emissions. It is well known that given current observational constraints and modelling limitations the monitoring of anthropogenic CO₂ emissions with such a system is extremely challenging. Whilst further developments are in progress to meet this eventual goal, initial demonstrations have been performed using other trace gases. The two species chosen here, CH₄ and NO_x, have better observational coverage and accuracy, and provide a signal-to-noise ratio sufficient to optimise anthropogenic emissions using the 24-hour window. Additionally, biogenic emissions are typically smaller for these species, which makes the inversion less prone to source misattribution. Finally, we have attempted to optimise CO₂

fluxes using a crude approximation (detailed below) of the error correlations between NO_x and CO₂. Note that these are preliminary results and require further development.

5.1 Demonstration using CH₄

Several case studies have been selected to demonstrate the capability of the system to monitor CH₄ emissions at a range of spatial and temporal scales. A schematic of the system is provided in Fig. 9, highlighting the model resolution and joint optimisation of initial 3D-state and emissions.

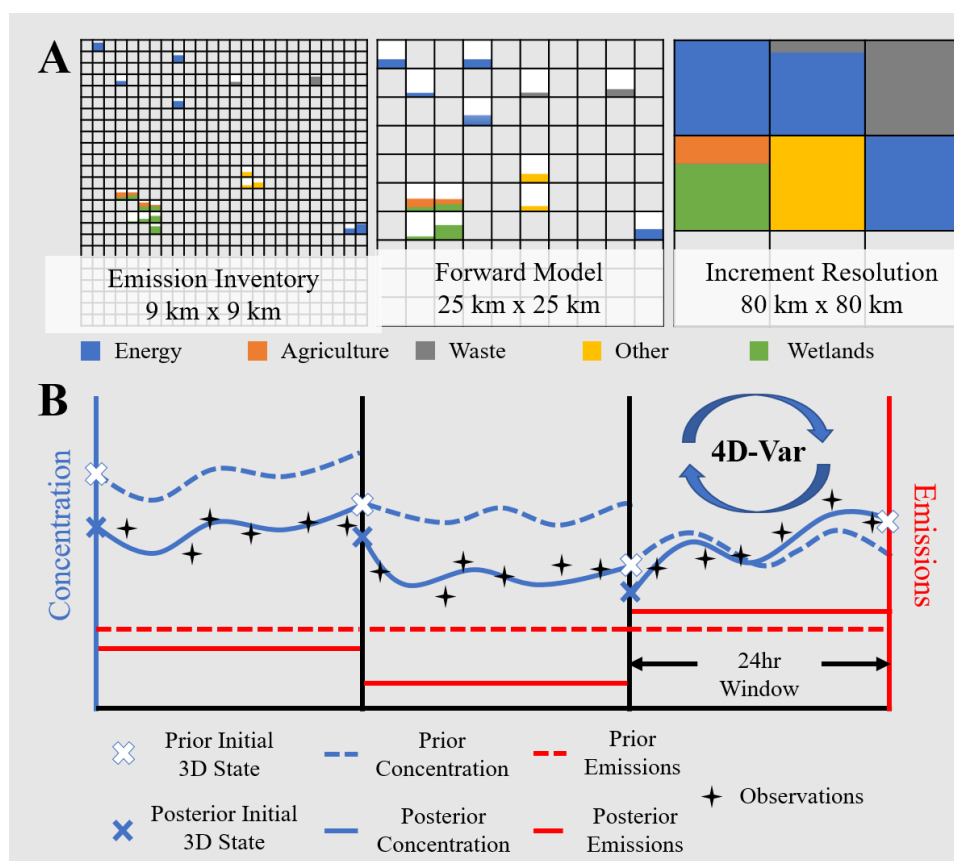


Figure 9 Schematic of different resolutions used in the inversion shown by pseudo-data for 5 sectors. The magnitude of prior emissions at ~9 km (left) and as input to the forward model at ~25 km (middle). The inversion increment at ~80 km, resulting scaling factors are applied to all sectors within the grid cell, the boxes indicate relative contribution per sector (right). b) Schematic of inversion setup using the 24-hour window, correcting for the initial 3D state, emissions, and initial conditions in the prior of the subsequent window. (McNorton et al., 2022).

A full description of all simulations, case studies and associated caveats are provided in McNorton et al. (2022), but in brief, the inversions were performed for the first half of 2019 and 2020. The model setup was based upon the operational GHG forecast (Agusti-Panareda et al., 2019) using the CAMS global emission product. Observations used in the inversion were provided by GOSAT, IASI and TROPOMI. The results were evaluated against TCCON observations and showed improvements of the modeled posterior atmospheric methane concentrations when emissions were optimised compared to a state-only optimisation.

5.1.1 Regional Emissions – Permian Basin, USA

The Permian Basin, an area of ~400km², is the largest oil-producing basin in the USA. Previous studies identified an underestimation in inventory estimates of CH₄ fluxes in this

region (Alvarez et al., 2018; Robertson et al., 2020; Zhang et al., 2020). Using only dates when nearby TROPOMI observations were available (237/485), inversions for the 15 months available (January to June 2019 and January to September 2020) provided average posterior emissions of 2.3 ± 0.5 Tg yr⁻¹ over the $6^\circ \times 4^\circ$ domain, centred around 32°N , 103°W (Figure 10). This is a considerable increase from the prior of 2.0 Tg yr⁻¹. The estimated flux brings emissions closer to, but remains lower than, a recent 4D-Var inversion estimate of 2.9 ± 0.5 Tg yr⁻¹ (Zhang et al., 2020). While it is difficult to diagnose the cause of the difference in posterior estimates, one possibility is the larger prior uncertainty used in Zhang et al. (2020). Additionally, transport uncertainties associated with initial meteorological conditions are accounted for in our online inversion system, which might significantly impact the derived emissions.

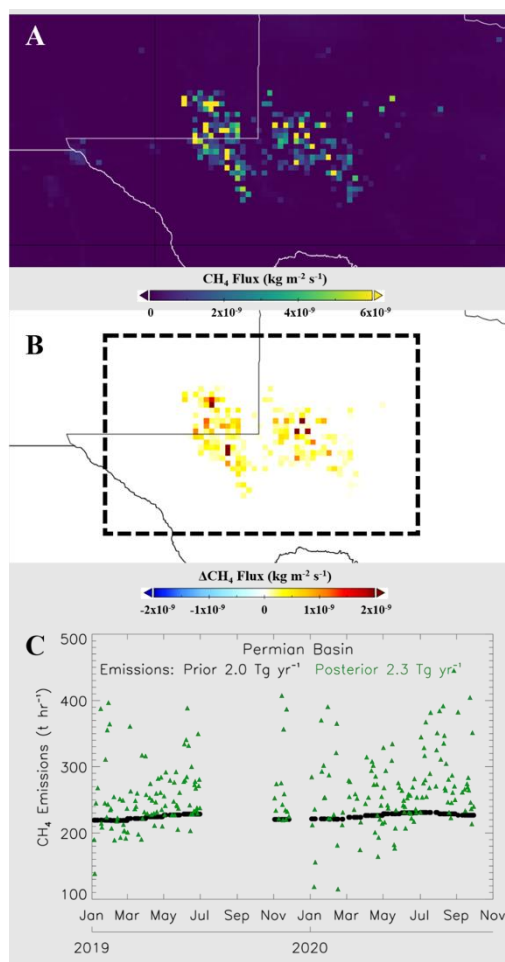


Figure 10 a) Average prior Permian Basin CH₄ emissions for 2019. b) Average of posterior minus prior anthropogenic CH₄ emissions over the Permian Basin for January-June 2019, excluding days for which observations were not available. c) Time series of total prior (black circles) and posterior (green triangles) anthropogenic CH₄ emission estimates within the $6^\circ \times 4^\circ$ Permian Basin domain, centered around 32°N , 103°W (black box in b) for 2019-2020, excluding days for which observations were not available. (McNorton et al., 2022)

5.1.2 Point Source Emissions – Appin Colliery, Australia

The Appin Colliery (34.2°S , 150.8°E), in New South Wales, Australia is an underground coal mine previously noted for having high CH₄ emissions (Varon et al., 2020). It represents a single point source, which is challenging to quantify as there are several nearby emission sources including landfills, dairy facilities, and a gas processing plant. Varon et al., (2020) used the high-resolution GHGSat-D instrument and integrated mass enhancement (IME) and cross-sectional flux (CSF) methods calibrated with large eddy simulations to derive vent

emissions from the mine between 2016 and 2018. They estimated mean CH₄ emissions of 5.9 t hr⁻¹ (IME) and 5.0 t hr⁻¹ (CSF), lower than the prior used here (6.7±0.1 t hr⁻¹, fugitive only: 6.0±0.1 t hr⁻¹). We derived 2019-2020 average grid cell emissions of 6.4±0.7 t hr⁻¹. Assuming little or no change in emissions between their 2016-2018 study period and our 2019-2020 estimate, our derived, fugitive-only, emissions (5.7±0.6 t hr⁻¹) agree well with their findings (Fig. 11). For 2019, a business-as-usual year, which is nearer to the time period investigated in their study, fugitive emissions are even lower (5.3±0.7 t hr⁻¹). These results suggest our inversion can detect biases in the prior from point sources, given sufficient observations (100/485 days observed), a relatively large point source (>~5 t hr⁻¹) and a suitable prior uncertainty estimate.

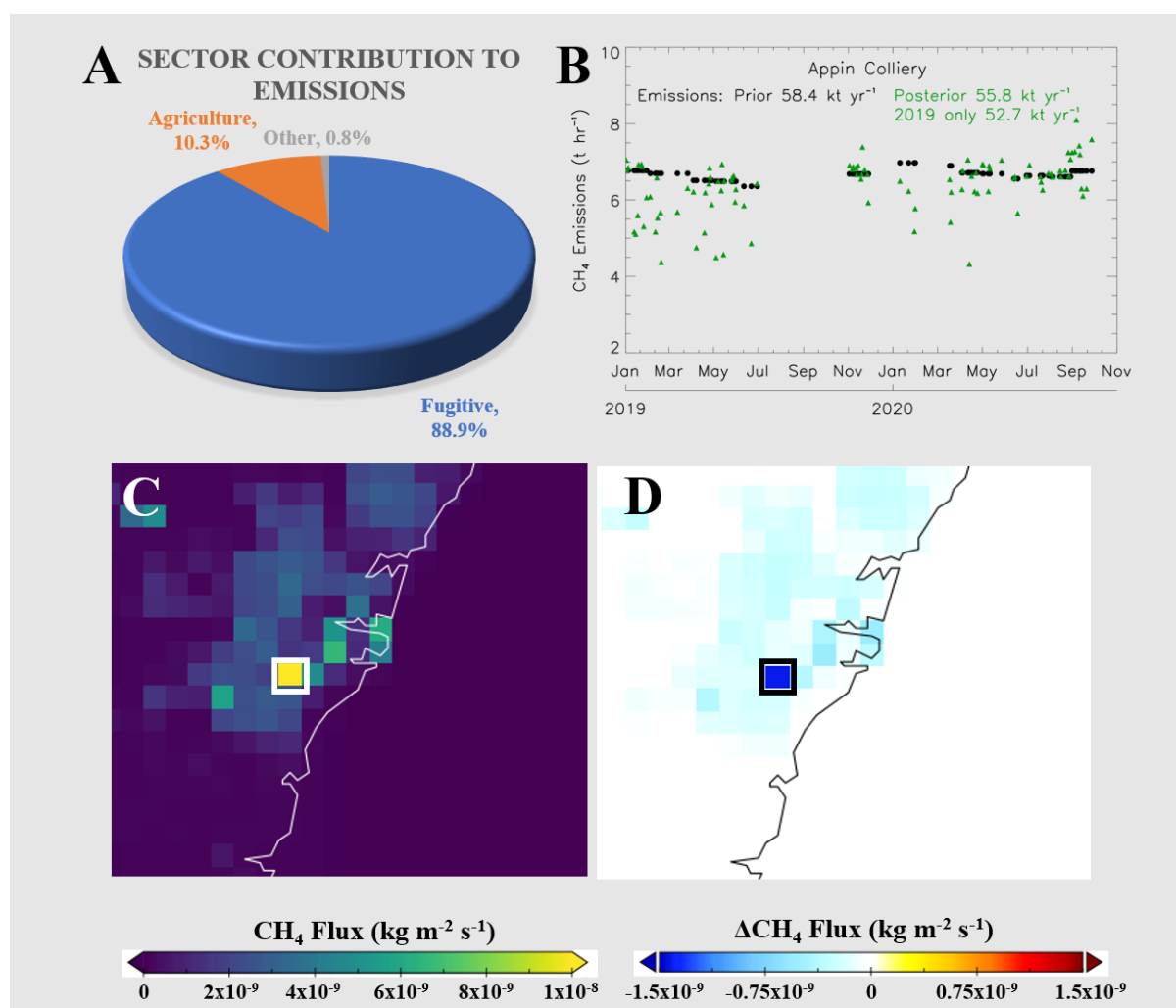


Figure 11 a) The sector specific contribution to emissions within the Appin Colliery domain. b) Time series of total prior (black circles) and posterior (green triangles) CH₄ emission estimates within the domain for 2019-2020, excluding days for which observations were not available. c) Prior CH₄ emissions for January 2019, the white box denotes the grid cell used to estimate emissions. d) Average posterior minus prior CH₄ emissions for 2019, excluding days for which observations were not available. (McNorton et al., 2022).

5.1.3 Blowout Event – Eagle Ford, USA

On 1st November 2019, a blowout event occurred at a gas well in the Eagle Ford Shale in Texas (28.9°N, 97.6°W), which was followed by a diminishing 20-day release event (Cusworth et al., 2021). Cusworth et al. (2021) estimated emissions of the blowout using several estimation techniques. Observations directly over the blowout were made from TROPOMI on

the 2nd, 3rd, 15th and 18th of November 2019. We further extended our analysis to all observations made between 15th October and 28th November 2019 within a 2°x2° domain centred around the blowout (Figure 12). We found when blowout emissions peaked on the 1st/2nd November 2019, posterior emissions at the site were ~40% higher than prior emissions; however, the magnitude of the posterior emissions (2.5 t hr⁻¹) is noticeably lower than the 28-61 t hr⁻¹ previously estimated (Cusworth et al., 2021). As expected, posterior emission estimates return to near prior levels after the initial blowout (Figure 12). Estimates provided by Cusworth et al., (2021) would require more than a 1,500% increase in emissions relative to our prior which is unlikely to be achieved with our relatively modest prior error (87%). It is likely given the model resolution and prior information that posterior emissions are incorrectly attributed to nearby grid cells. This is evident in the mapped scaling factors, which show increases incorrectly applied slightly to the west of the blowout location. Within a 4°x4° domain surrounding the blowout site posterior and prior emissions typically agree well for months excluding November, suggesting any differences occurring in November, could be attributed to the well blowout. Based on this assumption we used the residual from the posterior minus the prior to estimate blowout emissions on the 2nd November 2019 of 140 t hr⁻¹, which is more than double the estimate of Cusworth et al. (2021). These results suggest that the system, as presented here, can detect such events but cannot accurately quantify a well blowout of this magnitude over an oil field. It could however be used as a crude quantification of emissions from such a blowout over a larger domain, assuming other sources are well known. A more accurate quantification of emissions from release events of this nature, requires further development and possibly the implementation of alternative techniques that are better adapted for missing sources (e.g. Yu et al., 2021).

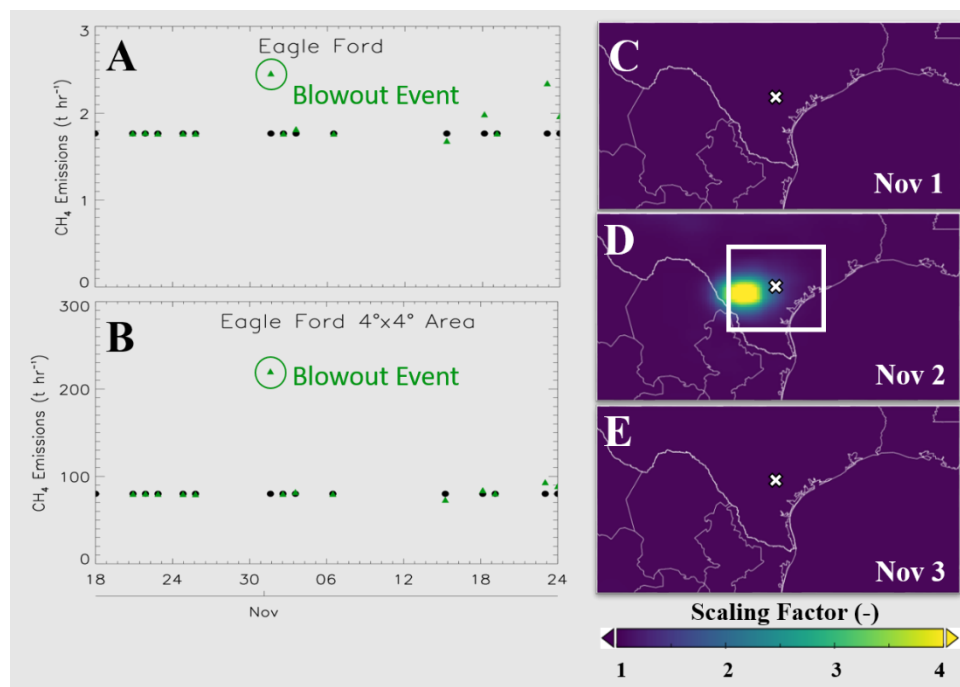


Figure 12 a) Prior (black circles) and Posterior (green triangles) anthropogenic CH₄ emission estimates, where observations are available, over an oil well blowout event in Eagle Ford, USA during October/November 2019 at the grid scale (a) and within a 4°x4° domain (b). The nearest date (2nd November) to the event, which occurred on the 1st November, is indicated. Regional scaling factor values from the inversion for November 1st (C), 2nd (D) and 3rd (E). Eagle Ford blowout site marked with an 'x' and 4°x4° domain denoted. (McNorton et al., 2022).

5.1.4 1-day Regional Emissions – Silesian Basin, Europe

The Upper Silesian Coal Basin (USCB) is one of the largest CH₄ emitting regions in Europe, with emissions originating from ~40 coal mines (EEA, 2021). The region extends from southern Poland across the border to Czechia where CH₄ is released from deep coal deposits and emitted to the atmosphere via ventilation shafts (Fiehn et al., 2020).

To evaluate the feasibility of the system to quantify regional CH₄ emission sources within a 24-hour window we performed a one-day inversion over the USCB. Results were compared with emission estimates derived using aircraft observations combined with Eulerian and Lagrangian dispersion models (Kostinek et al., 2021) and a mass balance approach (Fiehn et al., 2020). These studies used extensive flight data from the 6th June 2018 to derive regional CH₄ emission estimates of 0.42-0.48 Tg yr⁻¹. The CoMet v2 bottom-up inventory (Fiehn et al., 2020) was specifically compiled for the purpose of the flight campaign and estimated emissions in the region of 0.58 Tg yr⁻¹. Our results for the 6th of June 2018 estimated USCB emissions of 0.57 Tg yr⁻¹, compared to our prior estimate of 0.63 Tg yr⁻¹ (Figure 13). This shows good agreement with Carbon Dioxide and Methane Mission (CoMet) v2 and an improved agreement with the top-down estimates.

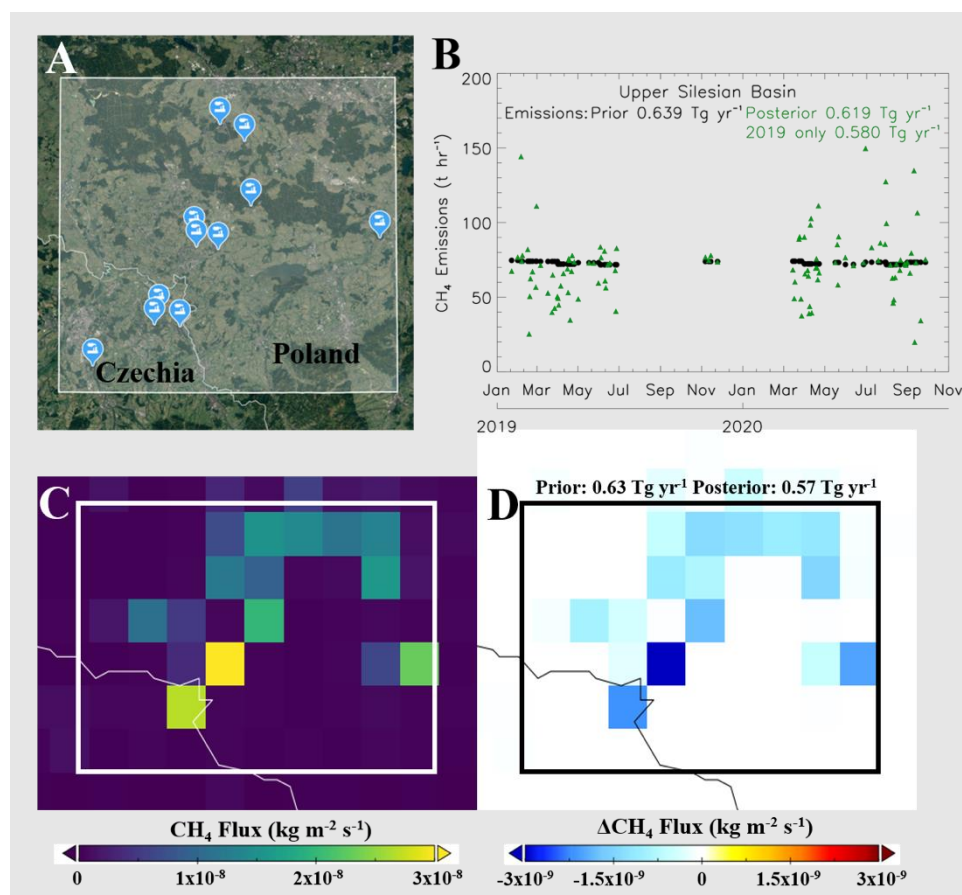


Figure 13 a) The Upper Silesian Coal Basin 1°x0.5° domain indicated by the white box, centred around 50.0°N, 18.7°E. Also shown are eleven major coal mines in the region (© Google Maps, 2021). b) Time series of total prior (black circles) and posterior (green triangles) CH₄ emission estimates within the domain for 2019-2020, where observations and inverse simulations were available. c) Prior total CH₄ emissions for 6th June 2018. d) Average posterior minus prior CH₄ emissions for 6th June 2018. (McNorton et al., 2022).

5.1.5 The Impact of Covid-19 on Emissions

To evaluate the impact on anthropogenic CH₄ emissions from the global slowdown, caused by the COVID-19 pandemic, we compared posterior emissions from January to June of 2019 and 2020. Globally, average anthropogenic emissions for the 6-month period in 2020 ($359.5 \pm 22.0 \text{ Tg yr}^{-1}$) are found to be 1.6% higher than for 2019 ($353.9 \pm 23.5 \text{ Tg yr}^{-1}$) (Fig. 14). These increased emissions contributed to the observed increased atmospheric growth rate between 2019 (10.0 ppb yr^{-1}) and 2020 (14.7 ppb yr^{-1}) (NOAA, 2021). Sector specific attribution shows the energy ($+2.7 \pm 1.6 \text{ Tg yr}^{-1}$) and agriculture ($+2.0 \pm 0.5 \text{ Tg yr}^{-1}$) sectors are the largest contributors to this increase, with smaller contributions from the waste ($+0.6 \pm 0.4 \text{ Tg yr}^{-1}$) and other anthropogenic sources ($0.4 \pm 0.2 \text{ Tg yr}^{-1}$).

When compared with 2019, anthropogenic CH₄ emissions in 2020 were larger pre-slowdown (January-February: $+5.6 \pm 0.0 \text{ Tg yr}^{-1}$), considerably larger during the early stages of the slowdown (March-April: $+8.2 \pm 0.9 \text{ Tg yr}^{-1}$) and only slightly larger in the latter months of the initial slowdown (May-June: $+3.2 \pm 0.0 \text{ Tg yr}^{-1}$). This suggests, globally, the impact of the slowdown initially increased emissions and subsequently reduced them, although emissions for all 6 months were higher in 2020 than for 2019. This trend in emissions was mainly driven by energy sector emissions (January-February: $+2.4 \text{ Tg yr}^{-1}$, March-April: $+4.7 \text{ Tg yr}^{-1}$, May-June: $+0.9 \text{ Tg yr}^{-1}$), whilst the agricultural sector showed a relatively consistent increase, relative to 2019, for all months.

When averaged over all 6 months, an increase in emissions between 2019 and 2020 was estimated in 6 out of 8 of the largest emitting regions, with the only exceptions being Pakistan (-0.0 Tg yr^{-1}) and Brazil (-0.28 Tg yr^{-1}). The largest increase was in China ($+2.6 \text{ Tg yr}^{-1}$), of which, over half originated from the energy sector, specifically from the northern coal mining regions. The difference in emissions from China, relative to 2019, were the main driver for the global trend with increases pre-slowdown (January-February: $+3.9 \text{ Tg yr}^{-1}$), large increases during the initial slowdown (March-April: $+6.0 \text{ Tg yr}^{-1}$) and only small increases in the latter months (May-June: $+1.4 \text{ Tg yr}^{-1}$). As with the global signal, this monthly variability is attributed to changes in energy sector emissions.

A limitation of the current system is the use of a climatological OH sink, which is the primary oxidant for atmospheric CH₄. Currently, OH is not included in the control vector and does not respond to changes in atmospheric chemistry. Formation pathways of OH are influenced by atmospheric NO_x concentrations, which were estimated to have decreased during the period (Dombia et al., 2021). Several simulations were performed using multiple chemistry schemes to assess the atmospheric impact of OH when using an adjusted emission scenario (Huijnen et al., 2021). Results show global OH decreases of 1-3% during the period, however a heterogeneous spatial pattern is observed near the surface with increased OH concentrations over some regions. This would suggest the 2020 increased emissions found here may be overestimated; however, the derived emission increases in January and February of 2020, relative to 2019, are unlikely to have been influenced by OH changes caused by the global COVID-19 lockdown. Future developments will include the addition of OH in the control vector and the use of an online OH loss rate derived using atmospheric chemistry, resulting in more accurate source/sink attribution.

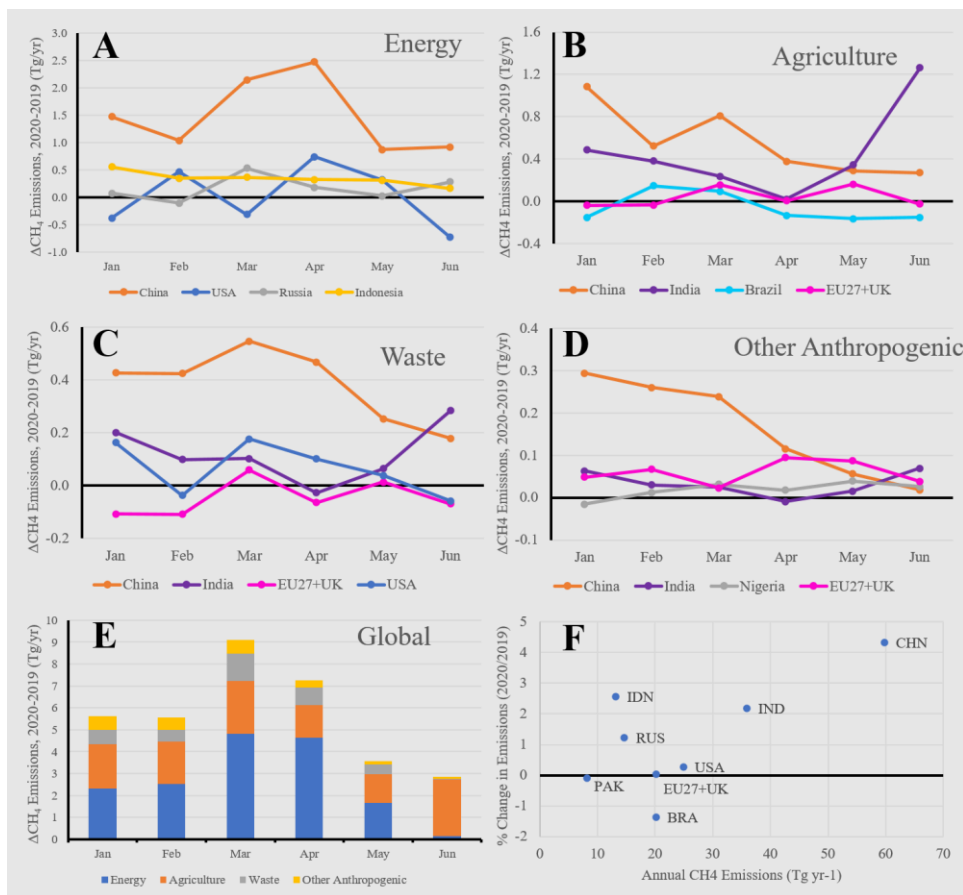


Figure 14 Estimated national/regional average CH₄ emission change between 2020 and 2019 for January to June, derived using an IFS inversion for the largest emitters for a) Energy, b) Agriculture, c) Waste and d) Other Anthropogenic sources. e) Global change in sector specific monthly CH₄ emissions for the same period. f) National/regional change in total anthropogenic CH₄ emissions for the same period. (McNorton et al., 2022).

5.2 Demonstration Using NO_x

To complement the work done in WP4 and described by D4.1, several case studies were used to demonstrate the global inversion system, in its current form, when considering NO_x and the co-emission relationship between NO_x and CO₂. Here, we focus on NO_x emissions from the Bełchatów Power Station case, but work is on-going to extend this to the other two sites, Jämschwalde Power Station and Berlin and for CO₂ emissions (Figure 15).

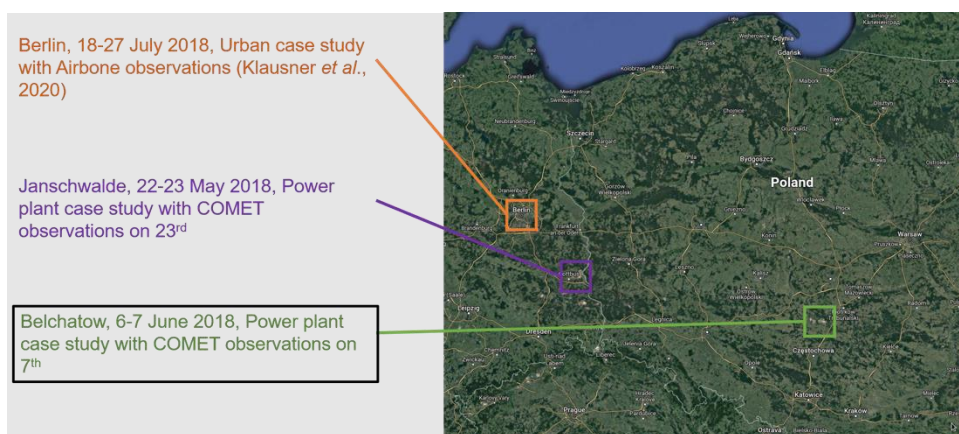


Figure 15 Map of the 3 case studies highlighted in WP4 for investigation (© Google Maps, 2021).

The Bełchatów Power Station, Poland, is one of the largest coal-fired power stations in the world. It was recently used as a case study for the CoMet measurement campaign, which included airborne in-situ measurements of multiple chemical species and meteorological variables. Observations were made on 07-06-2018 and simulations were performed between 3-12 June, 2018. For the initial simulation we assume no correlation between CO₂ and NO_x emissions with constraints only by respective observations of each species. Simulations were performed at ~40km horizontal resolution, with a coarser increment resolution (~80km), 3-hourly output and using operational CAMS emissions. Observations included the full suite of operational observations and included OMI XNO₂ and OCO-2 XCO₂ column products. Evaluation of the system using flux estimates derived from CoMet measurements will be performed in the next phase of the project when estimates become available.

5.2.1 NO_x Emissions – Bełchatów Power Station, Poland

Simulated total column NO₂ for the 7th June, 2018, shows the diurnal variability and a small plume enhancement over Bełchatów (Fig. 16). Given the coarse forward model resolution, the magnitude of the plume is expected to be small when compared with high-resolution regional models used in WP4. Additionally, unlike the regional WP4 models, the current version of the prototype does not include stack height in the emissions. This would further alter the modelled plume, an effect particularly notable from Bełchatów, which has two 299m high stacks.

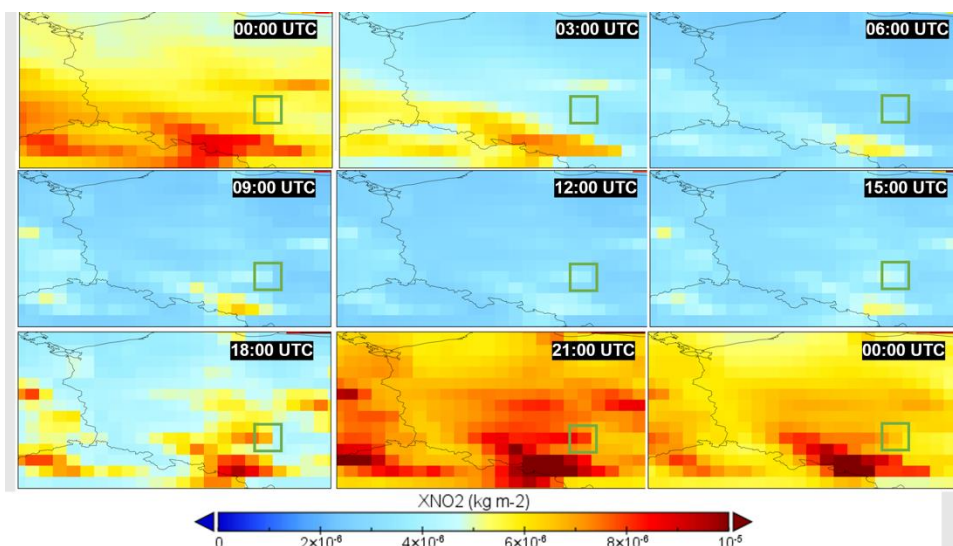


Figure 16 Simulated total column NO₂ for a 24-hour period (7th June, 2018) from the IFS global prototype over Western Poland. The green box denotes the location of the Bełchatów power station.

Although Bełchatów is a point source of NO_x in the CAMS inventory, emissions are gridded to ~9km resolution. At this resolution grid cell NO_x prior estimates of energy emissions are 1.95 t NO_x hr⁻¹. Emission increments at ~80km, applied to the native ~9km CAMS inventory, update these estimates on the 7th June, 2018 to 1.69 t NO_x hr⁻¹ (Fig. 17). This suggests emissions are over-estimated in the prior, at least for this day by ~13%, further investigation is required and validation with WP4 products will be performed in the future.

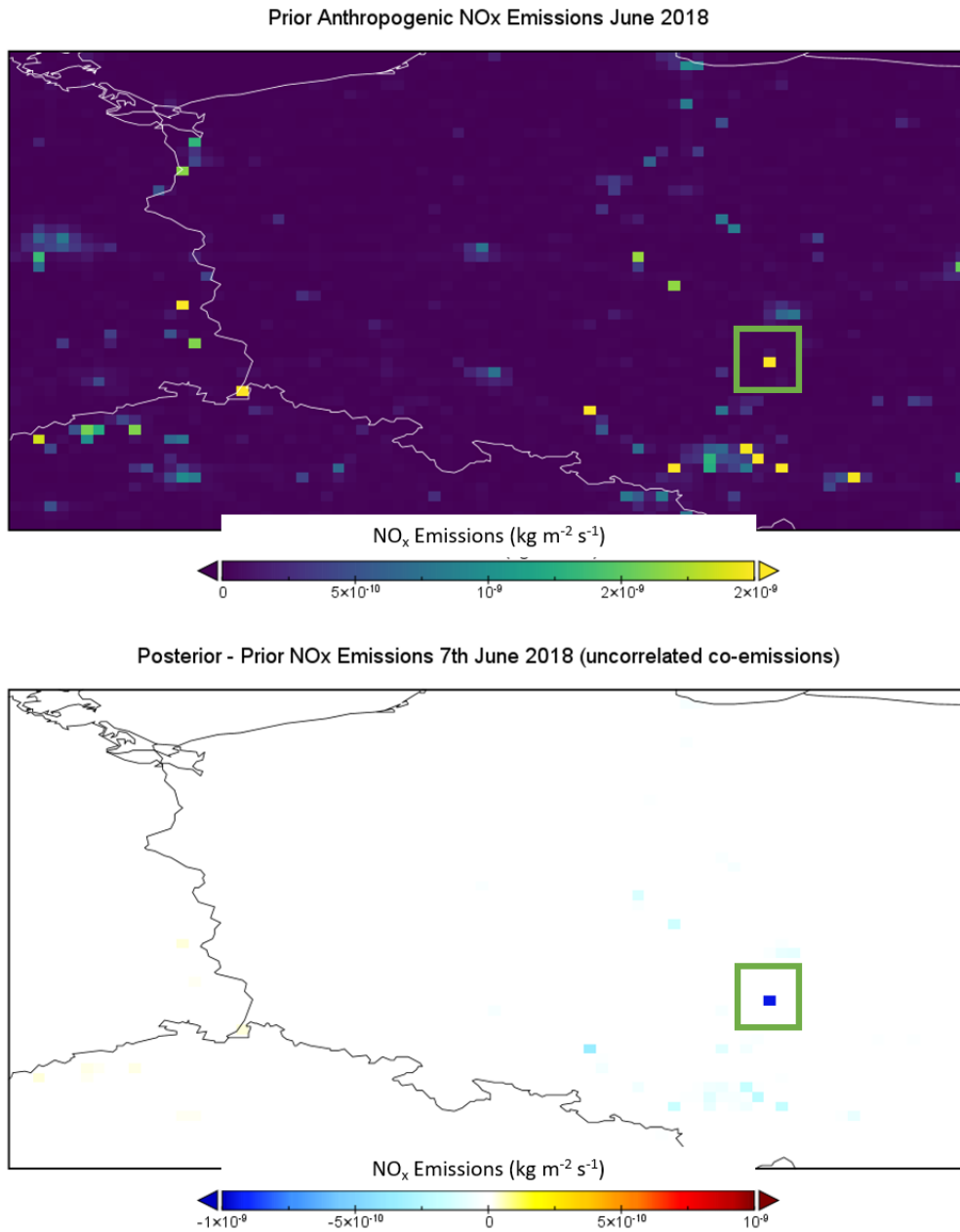


Figure 17 Prior anthropogenic NO_x emissions for Western Poland in June, 2018 taken from the CAMS inventory (top). The difference in NO_x emissions for the same region and period between inverse and prior estimates, when assuming no correlation between NO_x and CO₂ emissions (bottom). The green box denotes the location of the Bełchatów power station.

6 Conclusion

The main achievements in the development of the global CO₂ MVS based on the IFS during the first 12 months of the CoCO₂ project are listed below:

- New SL interpolation method COMADH performs much better than the current standard SL interpolation.
- Implementation of a simplified chemistry TL-AD in IFS analysis and inversion system.
- Demonstration of IFS inversion capability with CH₄ fluxes.

There is a lot of work in progress that will continue during the second year of the project including:

- Testing of COMADH tangent linear and adjoint code in the 4D-VAR system.
- Long-window (several weeks to a month) DA for CO₂ inversion based on the EDA.
- Work on specification of cross-species prior error correlation in collaboration with WP2.
- Improvement of point source representation in model in collaboration with WP2.
- Test higher model resolutions (4km) to improve representation of plumes

Future work will be required to further improve the global CO₂ MVS which will be addressed by future HE proposals. Below we list some recommendations for research priorities:

- Co-emitted species (to be addressed in Task 3.4 and CORSO project proposal).
- Development of efficient chemical model in the IFS analysis, for instance machine learning surrogate models.
- Implementation and testing in CAMS framework of a recently developed multi-tracer efficient SL advection scheme based on the accurate discontinuous Galerkin remapping, higher resolution testing, research in flux-form mass conserving advection schemes.

7 References

Agustí-Panareda, A., Diamantakis, M., Massart, S., Chevallier, F., Muñoz-Sabater, J., Barré, J., Curcoll, R., Engelen, R., Langerock, B., Law, R. M., Loh, Z., Morguá, J. A., Parrington, M., Peuch, V.-H., Ramonet, M., Roehl, C., Vermeulen, A. T., Warneke, T., and Wunch, D.: Modelling CO₂ weather – why horizontal resolution matters, *Atmos. Chem. Phys.*, 19, 7347–7376, <https://doi.org/10.5194/acp-19-7347-2019>, 2019.

Agusti-Panareda A., Diamantakis M., Bayona V., Klappenbach F., Butz A.: Improving the inter-hemispheric gradient of total column atmospheric CO₂ and CH₄ in simulations with the ECMWF semi-Lagrangian atmospheric global model, *Geoscientific Model Development* n. 1, pp. 1-18. DOI: 10.5194/gmd-10-1-2017, 2017.

Alvarez, R. A., Zavala-Araiza, D., Lyon, D. R., Allen, D. T., Barkley, Z. R., Brandt, A. R., Davis, K. J., Herndon, S. C., Jacob, D. J., Karion, A., Kort, E. A., Lamb, B. K., Lauvaux, T., Maasackers, J. D., Marchese, A. J., Omara, M., Pacala, S. W., Peischl, J., Robinson, A. L., Shepson, P. B., Sweeney, C., Townsend-Small, A., Wofsy, S. C., and Hamburg, S. P.: Assessment of methane emissions from the U.S. oil and gas supply chain, *Science*, eaar7204, <https://doi.org/10.1126/science.aar7204>, 2018.

Brunner, D., Kuhlmann, G., Marshall, J., Clément, V., Fuhrer, O., Broquet, G., Löscher, A., and Meijer, Y.: Accounting for the vertical distribution of emissions in atmospheric CO₂ simulations, *Atmos. Chem. Phys.*, 19, 4541–4559, <https://doi.org/10.5194/acp-19-4541-2019>, 2019.

Cheewaphongphan, P., Chatani, S., and Saigusa, N.: Exploring Gaps between Bottom-Up and Top-Down Emission Estimates Based on Uncertainties in Multiple Emission Inventories: A Case Study on CH₄ Emissions in China, *Sustainability*, 11, 2054, <https://doi.org/10.3390/su11072054>, 2019.

Cusworth, D. H., Duren, R. M., Thorpe, A. K., Pandey, S., Maasackers, J. D., Aben, I., Jarvis, D., Varon, D. J., Jacob, D. J., Randles, C. A., Gautam, R., Omara, M., Schade, G. W., Dennison, P. E., Frankenberg, C., Gordon, D., Lopinto, E., and Miller, C. E.: Multisatellite Imaging of a Gas Well Blowout Enables Quantification of Total Methane Emissions, *Geophys Res Lett*, 48, <https://doi.org/10.1029/2020gl090864>, 2021.

Deng, Z., Ciais, P., Tzompa-Sosa, Z. A., Saunois, M., Qiu, C., Tan, C., Sun, T., Ke, P., Cui, Y., Tanaka, K., Lin, X., Thompson, R. L., Tian, H., Yao, Y., Huang, Y., Lauerwald, R., Jain, A. K., Xu, X., Bastos, A., Sitch, S., Palmer, P. I., Lauvaux, T., d'Aspremont, A., Giron, C., Benoit, A., Poulter, B., Chang, J., Petrescu, A. M. R., Davis, S. J., Liu, Z., Grassi, G., Albergel, C. and Chevallier, F.: Comparing national greenhouse gas budgets reported in UNFCCC inventories against atmospheric inversions, *Earth Syst. Sci. Data*, [preprint], doi:10.5194/essd-2021-235, 2021.

Diamantakis M., Flemming J.: Global mass fixer algorithms for conservative tracer transport in the ECMWF model, *Geoscientific Model Development* n. 3, pp. 965-979. DOI: 10.5194/gmd-7-965-2014, 2014.

Michail Diamantakis, Anna Agusti-Panareda: A positive definite tracer mass fixer for high resolution weather and atmospheric composition forecasts, *ECMWF Technical Memoranda* n. 819. DOI: 10.21957/qpogzoy, 2017.

Doumbia, T., Granier, C., Elguindi, N., Bouarar, I., Darras, S., Brasseur, G., Gaubert, B., Liu, Y., Shi, X., Stavrou, T., Tilmes, S., Lacey, F., Deroubaix, A., and Wang, T.: Changes in global air pollutant emissions during the COVID-19 pandemic: a dataset for atmospheric modeling, *Earth Syst. Sci. Data*, 13, 4191–4206, <https://doi.org/10.5194/essd-13-4191-2021>, 2021.

Fiehn, A., Kostinek, J., Eckl, M., Klausner, T., Gałkowski, M., Chen, J., Gerbig, C., Röckmann, T., Maazallahi, H., Schmidt, M., Korbeń, P., Nečki, J., Jagoda, P., Wildmann, N., Mallaun, C., Bun, R., Nickl, A.-L., Jöckel, P., Fix, A., and Roiger, A.: Estimating CH₄, CO₂ and CO emissions from coal mining and industrial activities in the Upper Silesian Coal Basin using an aircraft-based mass balance approach, *Atmos. Chem. Phys.*, 20, 12675–12695, <https://doi.org/10.5194/acp-20-12675-2020>, 2020.

Guevara, M., Jorba, O., Tena, C., Denier van der Gon, H., Kuenen, J., Elguindi, N., Darras, S., Granier, C., and Pérez García-Pando, C.: Copernicus Atmosphere Monitoring Service TEMPORal profiles (CAMS-TEMPO): global and European emission temporal profile maps for atmospheric chemistry modelling, *Earth Syst. Sci. Data*, 13, 367–404, <https://doi.org/10.5194/essd-13-367-2021>, 2021.

Huijnen, V., Bouarar, I., Brasseur, G., Williams, J., Schreurs, T., and Remy, S.: Global trace gas changes in the IFS min-ensemble in response to changes in primary emissions during the COVID-19 pandemic, Copernicus Atmosphere Monitoring Service, 2021.

Klausner, T., Mertens, M., Huntrieser, H., Galkowski, M., Kuhlmann, G., Baumann, R., Roiger, A.: Urban greenhouse gas emissions from the Berlin area: a case study using airborne CO₂ and CH₄ in situ observations in summer 2018. *Elementa: Science of the Anthropocene*, 8, 15 (24 pp.). <https://doi.org/10.1525/elementa.411>, 2020.

Kostinek, J., Roiger, A., Eckl, M., Fiehn, A., Luther, A., Wildmann, N., Klausner, T., Fix, A., Knotte, C., Stohl, A., and Butz, A.: Estimating Upper Silesian coal mine methane emissions from airborne in situ observations and dispersion modeling, *Atmos. Chem. Phys.*, 21, 8791–8807, <https://doi.org/10.5194/acp-21-8791-2021>, 2021.

McNorton, J., Bousseres, N., Agustí-Panareda, A., Balsamo, G., Engelen, R., Huijnen, V., Inness, A., Kipling, Z., Parrington, M., and Ribas, R.: Quantification of methane emissions

from hotspots and during COVID-19 using a global atmospheric inversion, *Atmos. Chem. Phys. Discuss.* [preprint], <https://doi.org/10.5194/acp-2021-1056>, in review, 2022.

Liu, Y., Gruber, N., and Brunner, D.: Spatiotemporal patterns of the fossil-fuel CO₂ signal in central Europe: results from a high-resolution atmospheric transport model, *Atmos. Chem. Phys.*, 17, 14145–14169, <https://doi.org/10.5194/acp-17-14145-2017>, 2017.

Robertson, A. M., Edie, R., Field, R. A., Lyon, D., McVay, R., Omara, M., Zavala-Araiza, D., and Murphy, S. M.: New Mexico Permian Basin Measured Well Pad Methane Emissions Are a Factor of 5–9 Times Higher Than U.S. EPA Estimates, *Environ. Sci. Technol.*, 54, 13926–13934, <https://doi.org/10.1021/acs.est.0c02927>, 2020.

Varon, D. J., Jacob, D. J., Jervis, D., and McKeever, J.: Quantifying Time-Averaged Methane Emissions from Individual Coal Mine Vents with GHGSat-D Satellite Observations, *Environ. Sci. Technol.*, 54, 10246–10253, <https://doi.org/10.1021/acs.est.0c01213>, 2020.

Zhang, Y., Gautam, R., Pandey, S., Omara, M., Maasackers, J. D., Sadavarte, P., Lyon, D., Nesser, H., Sulprizio, M. P., Varon, D. J., Zhang, R., Houweling, S., Zavala-Araiza, D., Alvarez, R. A., Lorente, A., Hamburg, S. P., Aben, I., and Jacob, D. J.: Quantifying methane emissions from the largest oil-producing basin in the United States from space, *Sci. Adv.*, 6, <https://doi.org/10.1126/sciadv.aaz5120>, 2020.

Document History

| Version | Author(s) | Date | Changes |
|---------|----------------------------|------------|---|
| 0.1 | ECMWF | 17/01/2021 | |
| 1.0 | Richard Engelen (ECMWF) | 25/02/2022 | Decided to finalise this version of the document by considering all minor comments. All comments and recommendations that require additional work or significant additional text will be added in an updated version to be released by 15 April 2022 latest to enable a well thought through final version of the document. |

Internal Review History

| Internal Reviewers | Date | Comments |
|--------------------------------------|------------|---|
| Name (Organisation) | dd/mm/yyyy | |
| Maarten Krol and Wouter Peters (WUR) | 17/01/2022 | |
| Dominik Brunner (EMPA) | 21/02/2022 | <ul style="list-style-type: none"> • Reorganize/renumber the last three sections • Add more information on the simplified chemistry TL/adjoint • Better explain the hybrid assimilation approach, especially in Section 4.1 • Consider my further remarks and corrections in the annotated document |
| Thomas Kaminski (iLab) | 21/02/2022 | Overall, I think the work that has been performed is impressive. Several recommendations for further work have been made offline. |

Estimated Effort Contribution per Partner

| Partner | Effort |
|--------------|-------------------|
| ECMWF | 15 |
| BSC | 2 |
| TNO | 0 (advisory role) |
| Total | 17 |

This publication reflects the views only of the author, and the Commission cannot be held responsible for any use which may be made of the information contained therein.